ARMY RESEARCH LABORATORY

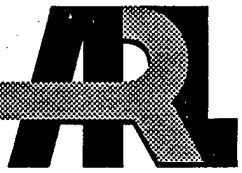

Reacting Flow Simulation for a Large-Scale Ram Accelerator

Michael J. Nusca

ARL-TR-966 February 1996

NOTICES

Destroy this report when it is no longer needed. DO NOT return it to the originator.

Additional copies of this report may be obtained from the National Technical Information Service, U.S. Department of Commerce, 5285 Port Royal Road, Springfield, VA 22161.

The findings of this report are not to be construed as an official Department of the Army position, unless so designated by other authorized documents.

The use of trade names or manufacturers' names in this report does not constitute indorsement of any commercial product.

REPORT DOCUMENTATION PAGE

Form Approved
OMB No. 0704-0188

1. AGENCY USE ONLY *(Leave blank)*	2. REPORT DATE	3. REPORT TYPE AND DATES COVERED
	February 1996	Final Jan - Dec 1994

4. TITLE AND SUBTITLE

Reacting Flow Simulation for a Large-Scale Ram Accelerator

5. FUNDING NUMBERS

PR: 1L162618A1FL

6. AUTHOR(S)

Michael J. Nusca

7. PERFORMING ORGANIZATION NAME(S) AND ADDRESS(ES)

U.S. Army Research Laboratory
ATTN: AMSRL-WT-PA
Aberdeen Proving Ground, MD 21005-5066

8. PERFORMING ORGANIZATION REPORT NUMBER

ARL-TR-966

9. SPONSORING/MONITORING AGENCY NAMES(S) AND ADDRESS(ES)

10.SPONSORING/MONITORING AGENCY REPORT NUMBER

11. SUPPLEMENTARY NOTES

12a. DISTRIBUTION/AVAILABILITY STATEMENT

Approved for public release; distribution is unlimited.

12b. DISTRIBUTION CODE

13. ABSTRACT *(Maximum 200 words)*

Computational fluid dynamics solutions of the full Navier-Stokes equations have been used to numerically simulate the reacting in-bore flow field for the ram accelerator projectile propulsion system. In this system, a projectile and obturator are injected at supersonic velocity into a stationary tube filled with a pressurized mixture of hydrocarbon, oxidizer, and inert gases. Flow stagnation on the obturator initiates combustion of the mixture before it is discarded. A system of shock waves on the projectile, in conjunction with viscous heating, sustains combustion. The resulting energy release travels with the projectile. Numerical simulation utilizing finite-rate chemical kinetics has been used to visualize the flow field, predict the effects of variation in system parameters, and predict projectile in-bore velocity.

14. SUBJECT TERMS

Navier-Stokes, computational fluid dynamics, reacting flow, detonation, kinetics

15. NUMBER OF PAGES

37

16. PRICE CODE

17. SECURITY CLASSIFICATION OF REPORT	18. SECURITY CLASSIFICATION OF THIS PAGE	19. SECURITY CLASSIFICATION OF ABSTRACT	20. LIMITATION OF ABSTRACT
UNCLASSIFIED	UNCLASSIFIED	UNCLASSIFIED	UL

INTENTIONALLY LEFT BLANK.

ACKNOWLEDGMENTS

Mr. Albert Horst and Dr. Thomas Minor have supported both the experimental and numerical simulation aspects for the Hybrid In-Bore RAM (HIRAM) project since its inception and have contributed to this work through various technical discussions. Drs. S. Palaniswamy and S. Chakravarthy, Rockwell Science Center, provided numerous points of technical assistance with the Unified Solution Algorithm Real Gas (USA-RG) code.

INTENTIONALLY LEFT BLANK.

TABLE OF CONTENTS

INTENTIONALLY LEFT BLANK.

LIST OF FIGURES

INTENTIONALLY LEFT BLANK.

1. INTRODUCTION

Experimental testing and gasdynamic modeling of the ram acceleration technique for in-bore projectile propulsion are being investigated at the U.S. Army Research Laboratory (ARL) under the Hybrid In-Bore RAM (HIRAM) propulsion program (Kruczynski 1994a, 1994b; Nusca 1994a, 1994b; Liberatore 1994). This research program seeks to provide a highly efficient method of achieving hypervelocity (≥2 km/s) projectile gun-launch for use in high-speed impact testing applications. The ARL ram accelerator system uses a 120-mm (bore diameter) tube that is modeled after the 38-mm system at the University of Washington (Hertzberg, Bruckner, and Bogdanoff 1988), where the technology was first demonstrated. Ram acceleration technology has also been successfully demonstrated at the Institute of St. Louis (ISL) in France (Giraud, Legendre, and Simon 1991; Smeets et al. 1994).

Numerical solutions of the Navier-Stokes equations have been obtained at the ARL via computational fluid dynamics (CFD) for nonreacting and reacting, two- and three-dimensional (2-D and 3-D) flows. These codes are being used to investigate the complex gasdynamic physics of ram accelerator projectile propulsion. A variety of CFD techniques have been brought to bear on this problem, including models for chemically frozen (nonreacting) gas, finite-rate global and multiple step chemical kinetics, and equilibrium chemical processes. Accurate numerical simulation of hydrocarbon-based reacting flow creates a very great demand on computational resources since the number of intermediate species and the number of kinetic steps for typical hydrocarbon fuels are prohibitively large. Global reaction mechanisms based on up to three steps have therefore been investigated for use in preliminary design studies. Using supercomputers, viscous and chemically reacting gasdynamic simulations can be used within hours to assess the influence of projectile velocity, tube fill pressure and mixture composition, and projectile geometry on species consumption, tube wall pressure and projectile thrust. These studies are being used to seek optimum performance for the ARL ram accelerator with minimal gun firings.

The ARL ram accelerator facility, projectile, operation, and experimental results have been reviewed by Kruczynski and are not repeated in this report (see Kruczynski 1994a).

2. REACTING FLOW MODEL

CFD flow simulations for the ARL ram accelerator are performed using the Rockwell Science Center Unified Solution Algorithm Real Gas (USA-RG) code (Chakravarthy et al. 1985; Palaniswamy and Chakravarthy 1989; Palaniswamy, Ota, and Chakravarthy 1991). This CFD code solves the full, 3-D,

unsteady Reynolds-Averaged Navier-Stokes (RANS) equations including equations for chemical kinetics (finite-rate and equilibrium). These partial differential equations are cast in conservation form and converted to algebraic equations using an upwind finite-volume formulation. Solution takes place on a mesh of nodes distributed in a zonal fashion around the projectile and throughout the flow field such that sharp geometric corners and other details are accurately represented. The conservation law form of the equations assures that the end states of regions of discontinuity (shocks, detonations, deflagrations) are physically correct even when smeared over a few computational cells. The Total Variation Diminishing (TVD) technique is employed to discretize inertia terms of the conservation equations, while the viscous terms are evaluated using an unbiased stencil. Flux computations across cell boundaries are based on Roe's (1981) scheme for hyperbolic equations. Spatial accuracy of third-order can be maintained in regions of the flow field with continuous variation, while slope limiting, used near large flow gradients, reduces the accuracy locally to avoid spurious oscillations.

Previous investigators have used CFD to simulate ram accelerator flow fields. In each case, CFD was used to solve the Navier-Stokes equations for the chemically reacting flow field in the accelerator tube around the projectile. Differences in CFD analysis arise from choices of numerical solution/discretization algorithm, representation of the turbulence terms, equation of state, and chemical kinetics scheme. Soetrisno (Soetrisno, Imlay, and Roberts 1992) used the LU-SGS implicit finite-volume method (flux-vector splitting and symmetric TVD) with an approximate diagonal chemical source term Jacobian, algebraic turbulence model, perfect-gas equation of state, and a quasi-global, 9-species/12-reaction, methane-oxygen finite-rate kinetics model. Yungster (Yungster and Rabinowitz 1994) used the LU-SSOR implicit finite-volume method (implicit factorization and symmetric TVD) with a full chemical source term Jacobian, algebraic turbulence model, perfect-gas equation of state, and a 20-species/52-reaction, finite-rate kinetics model. Li (Li et al. 1992) used the Flux-Corrected Transport (FCT) explicit finite-volume method with a noninertial source term to account for projectile acceleration, inviscid flow model, perfect-gas equation of state, and a simplified two-step parametric hydrogen-air kinetics model (induction step followed by energy release step). Hosangadi (Hosangadi et al. 1993) used the Roe/TVD upwind implicit finite-volume method (Riemann scheme modified for multiphase flows) with a fully-coupled chemical source term Jacobian, two-equation and large-eddy turbulence models, virial equation of state, and a quasi-global, 9-species/12-reaction finite-rate kinetics model.

The RANS equations for 2-D/axisymmetric reacting flow (N species mixture) are written in the following conservation form (Palaniswamy, Ota, and Chakravarthy 1991):

$$\frac{\partial W}{\partial t} + \frac{\partial (F_1 - G_1)}{\partial x} + \frac{\partial (F_2 - G_2)}{\partial y} + \frac{\alpha (F_2 - G_2)}{y} = \Omega \qquad (1)$$

$$W = (e, \rho, \rho u, \rho v, \rho \sigma_1, \ldots, \rho \sigma_{N-1})$$

$$F_1 = \left((e + p)u, \rho u, \rho u^2 + p, \rho uv, \rho u \sigma_1, \ldots, \rho u \sigma_{N-1}\right)$$

$$F_2 = \left((e + p)v, \rho v, \rho vu, \rho v^2 + p, \rho v \sigma_1, \ldots, \rho v \sigma_{N-1}\right)$$

$$G_1 = \left(\kappa_m \frac{\partial T}{\partial x} + \sum_i \rho D \left(h_i - h_N\right) \frac{\partial \sigma_i}{\partial x} + u\tau_{xx} + v\tau_{xy}, 0, \tau_{xx}, \tau_{xy}, \rho D \frac{\partial \sigma_i}{\partial x}, \ldots, \rho D \frac{\partial \sigma_{N-1}}{\partial x}\right)$$

$$G_2 = \left(\kappa_m \frac{\partial T}{\partial y} + \sum_i \rho D \left(h_i - h_N\right) \frac{\partial \sigma_i}{\partial y} + u\tau_{yx} + v\tau_{yy}, 0, \tau_{yx}, \tau_{yy}, \rho D \frac{\partial \sigma_i}{\partial y}, \ldots, \rho D \frac{\partial \sigma_{N-1}}{\partial y}\right)$$

$$\Omega = \left(0, 0, 0, \alpha\tau^+, \sum_k \omega_{1k}, \ldots, \sum_k \omega_{(N-1)k}\right).$$

The shear stress terms are given by

$$\tau_{yy} = 2\mu_m \frac{\partial v}{\partial y} - \frac{2}{3}\mu_m \left(\frac{\partial u}{\partial x} + \frac{\partial v}{\partial y} + \frac{v\alpha}{y}\right)$$

$$\tau_{xy} = \tau_{yx} = \mu_m\left(\frac{\partial u}{\partial y} + \frac{\partial v}{\partial x} + \frac{v\alpha}{y}\right)$$

$$\tau_{xx} = 2\mu_m\frac{\partial u}{\partial x} - \frac{2}{3}\mu_m\left(\frac{\partial u}{\partial x} + \frac{\partial v}{\partial y} + \frac{v\alpha}{y}\right)$$

$$\tau_{+} = 2\mu_m\frac{\alpha v}{y} - \frac{2}{3}\mu_m\left(\frac{\partial u}{\partial x} + \frac{\partial v}{\partial y} + \frac{v\alpha}{y}\right).$$

The species viscosity and thermal conductivity are referenced to μ_o, κ_o, and T_o using Sutherland's law,

$$\frac{\mu_i}{\mu_{oi}} = \left(\frac{T}{T_{o\mu}}\right)^{3/2}\frac{T_{o\mu} + S_\mu}{T + S_\mu}; \qquad \frac{\kappa_i}{\kappa_{oi}} = \left(\frac{T}{T_{o\kappa}}\right)^{3/2}\frac{T_{o\kappa} + S_\kappa}{T + S_\kappa}, \tag{2}$$

where T_o and S vary with species (Stull and Prophet 1971). The mixture viscosity and thermal conductivity are determined using Wilke's law (Wilke 1950) denoting f as μ or κ,

$$f_m = \sum_{i=1}^{N}\frac{X_i f_i}{\sum_{j=1}^{N} X_j\phi_{ij}}; \qquad \phi_{ij} = \frac{1}{\sqrt{8}}\left(1 + \frac{M_i}{M_j}\right)^{-1/2}\left[1 + \left(\frac{f_i}{f_j}\right)^{1/2}\left(\frac{M_j}{M_i}\right)^{1/4}\right]^2. \tag{3}$$

Fick's law is used to relate the mixture diffusivity to the mixture viscosity through the Schmidt number $Sc = \mu_m/(\rho D)$. The specific heat and enthalpy of each species (per mass) are given by the following fourth-order polynomial curve fits in terms of temperature, T, (Drummond, Rogers, and Hussaini 1987)

$$\frac{c_{p_i}}{R_i} = A_i + B_iT + C_iT^2 + D_iT^3 + E_iT^4 \tag{4}$$

$$h_i = R_i\left(A_i + \frac{B_i}{2}T + \frac{C_i}{3}T^2 + \frac{D_i}{4}T^3 + \frac{E_i}{5}T^4\right)T + \Delta H_{f_i} \tag{5}$$

$$\frac{g_i}{R_i} = A_i(T - \ln T) - \frac{B_i}{2}T^2 + \frac{C_i}{6}T^3 - \frac{D_i}{12}T^4 - \frac{E_i}{20}T^5 + \frac{\Delta H_{f_i}}{R_i} - F_i T. \tag{6}$$

The mixture enthalpy, total energy per unit volume, and ratio of specific heats are given by

$$h = \sum_{i=1}^{N} \sigma_i \int_{T_{p_i}} dT + \sum_{i=1}^{N} \sigma_i \Delta H_{f_i}; \qquad e = \frac{p}{\gamma - 1} + \rho\frac{(u^2 + v^2)}{2} + \sum_{i=1}^{N} \rho\sigma_i \Delta H_{f_i} \tag{7}$$

$$\gamma = 1 + \frac{1}{\dfrac{c_{pm}}{R_u \sum_i (\sigma_i/M_i)} - 1}; \qquad c_{pm} = \frac{1}{T}\sum_{i=1}^{N} \sigma_i \int^T C_{p_i} dT. \tag{8}$$

2.1 Equation of State. There are a number of formulas that have been proposed to describe the thermodynamic behavior for states where the deviations from a perfect gas are distinct (Gruschka and Wecken 1971). In most cases, the improvement starts from the perfect gas concept as the limiting case for small pressures and large specific volumes, adapting the formulas according to the observed behavior by means of suitable corrections.

$$p = \sum_{i=1}^{N} p_i = \rho T R_u \sum_{i=1}^{N} \frac{\sigma_i}{M_i} \tag{9}$$

Some of the best known examples are given below.

$$\left(p + \frac{a}{V^2}\right)(V - b) = nR_u T \qquad \text{(van der Waals)} \tag{10}$$

$$p(V - b) = nR_uT; \qquad b = \sum_i n_i b_i \qquad \text{(Abel)} \tag{11}$$

$$\frac{pV}{nR_uT} = 1 + \frac{B(T,n_i)}{V} + \frac{C(T,n_i)}{V^2} + \ldots \qquad \text{(Virial)} \tag{12}$$

Equations 10 and 11 are the simplest ways of taking into account the real gas effects using molecular attraction (a) and covolume (b). Equation 11 can be derived from the Virial equation (Equation 12) assuming very high temperatures and gas densities low enough that the mean volume available per molecule is large compared to the volume of the hard-sphere core of the molecule (Reif 1965). Equation 12 is very general and in principle exactly valid. The convergence of the series, however, is guaranteed only for moderately dense gases. For high densities in chemically reacting flows, the formula is practically of no use (Gruschka and Wecken 1971) unless the series is truncated and certain assumptions are made for B and C. Expressions for B and C, the second and third Virial coefficients, are given by (Smith and Van Ness 1987)

$$B = \sum_l \sum_m \sigma_l \sigma_m B_{lm}; \qquad C = \sum_l \sum_m \sum_n \sigma_l \sigma_m \sigma_n C_{lmn}. \tag{13}$$

For a binary mixture, these expressions reduce to

$$B = \sigma_1^2 B_{11} + 2\sigma_1\sigma_2 B_{12} + \sigma_2^2 B_{22}; \qquad C = \sigma_1^3 C_{111} + 3\sigma_1^2\sigma_2 C_{112} + 3\sigma_1\sigma_2^2 C_{122} + \sigma_2^3 C_{222}$$

Second and third pure coefficients (B_{11}, B_{22}, C_{111}, C_{222}), as well as cross-coefficients (B_{12}, C_{112}, C_{122}), are determined from experimental data that is, in general, available only for very limited applications (Smith and Van Ness 1987). Although B_{lm} and C_{lmn} are determinable in principle from intermolecular potential functions, these are rarely known accurately except for the simplest of molecules. The virial coefficients for pure species can be obtained experimentally from volumetric data, but those for species in solution are rarely available. It is thus usually necessary to postulate mixing rules relating the coefficients of the solution to the pure species. The main disadvantage of the virial equation is its inapplicability to high densities (Smith and Missen 1982). Hosangadi (Hosangadi et al. 1993) used the

Virial equation for ram accelerator flow fields and showed some effect in the location and strength of shock wave reflections. In these computations (for a multicomponent hydrocarbon mixture), the cross-coefficients for B and all coefficients for C were neglected; thus, C = 0 and $B = \Sigma_l \sigma_l B_l$. For the computations described in the present work, a covolume equation of state is used (Equation 11) where the covolume, b, for each species is obtained from Hirschfelder (Hirshfelder, Curtis, and Bird 1954).

2.2 Turbulence Models. The system of Navier-Stokes equations is valid for the laminar flow of a viscous, Newtonian fluid. In reality, the flow will remain laminar up to a certain critical value of the Reynolds number, $\rho U L/\mu$, where U and L are representative values of the velocity and length scales for the considered flow system. Above this critical value the flow becomes turbulent and is characterized by the appearance of fluctuations in all variables (velocity, pressure, density, temperature, etc.) around mean values. These fluctuations are statistical in nature and cannot be described in a deterministic way. However, they can be computed numerically using approaches such as large eddy simulations (LES) and Reynolds-Averaged Navier-Stokes (RANS) simulations.

LES uses a fixed spacial resolution, with the effects of unresolved turbulent eddies modeled using gradient transport methods such as eddy viscosity. RANS models all turbulent fluctuations theoretically or empirically, not just the ones smaller than the computational grid spacing. The RANS equations are derived by decomposing the dependent variables in the conservation equations into time mean (obtained over an appropriate time interval) and fluctuating components and then time averaging the entire equation. This time averaging is defined in such a way as to remove the influence of the turbulent fluctuations while not destroying the time dependence associated with other time-dependent phenomena with time scales distinct from those of turbulence. After substitution of these variables into the mass, momentum, and energy conservation equations and canceling terms that are identically zero, two types of stress terms are produced—laminar-like stress gradients for the mean motion and apparent stress gradients due to the transport of momentum by turbulent fluctuations. These apparent stresses are commonly called the Reynolds stresses. For first-order closure models, the Reynolds stresses are expressed in terms of an eddy viscosity, μ_t, resulting from the Boissineq assumption (Anderson, Tannehill, and Plethcher 1984). The Baldwin-Lomax model (Baldwin and Lomax 1978) describes the eddy viscosity using y_{max} as the value where Γ attains the value Γ_{max}, intermittency, F, and constants $\alpha = 0.3$, $\beta = 1.6$, $A = 26$.

$$\mu_t = 0.0168\beta F y_{max} \Gamma_{max}; \quad F = \left(1 + 5.5 \left(\frac{\alpha y}{y_{max}} \right)^6 \right)^{-1}; \quad \Gamma = y \left(1 - e^{-y^+/A} \right) \left| \frac{\partial u}{\partial y} - \frac{\partial v}{\partial x} \right| \qquad (14)$$

Where $y_+ = (y\rho/\mu)(\tau_{wall}/\rho)^{-1/2}$. This model has been used extensively for thin attached shear layers at moderate Mach numbers with acceptable results. However, when separation of the boundary layer is approached, poor predictions result. To improve the predictive capability of separated flows using RANS equations, a new turbulence model has been developed (Goldberg 1986). The model is based on experimental observations of detached flows. It prescribes turbulence kinetic energy and dissipation analytically within back flows. A formula for the eddy viscosity distribution within back flows is derived and used for the RANS equations when the calculations are done inside separation bubbles. Outside of them, the Baldwin-Lomax turbulence model (Baldwin and Lomax 1978) supplies the values of eddy viscosity. While the Baldwin-Lomax turbulence model is used to detect flow separation and to initiate application of the backflow model, the backflow model can relocate the separation point.

2.3 Chemical Reactions. Hydrocarbon reactions are commonly used for ram accelerator testing at ARL (Kruczynski 1994a). For example,

$$3CH_4 + 2O_2 + 10N_2 . \tag{15}$$

This reaction is one of a general class of hydrocarbon reactions investigated by Westbrook and Dryer (Westbrook and Dryer 1981)

$$C_aH_bO_c + \frac{1}{2}\left(a + \frac{b}{2} + c\right)O_2 \Rightarrow aCO + \frac{b}{2}H_2O . \tag{16}$$

The fuel equivalence ratio, ϕ, is a measure of the amount of fuel available for combustion. When $\phi = 1$, the proportions of fuel-to-oxygen are stoichiometric. For ϕ values smaller than unity, fuel should be completely consumed. For the reaction stated above, $\phi = 3.0$, which is considered outside the range of well understood CH_4/O_2 chemical kinetics, especially for $P \geq 10$ atm (Anderson and Kotlar 1991). Including all intermediate species and reaction steps for Equation 15, within the framework of a CFD calculation could be defeated by uncertainties in the thermodynamic, transport, and chemical-kinetic properties of these species especially at high pressures where these data have not been measured. In addition, the computational cost of a given reaction mechanism depends primarily on the number of

chemical species included, rather than the number of reactions (Westbrook and Dryer 1981). Such extensive kinetic mechanisms (12–19 species) have been included in CFD analyses using atmospheric pressure kinetics data (Yungster and Rabinowitz 1994). Given the above concerns, global reaction mechanisms for hydrocarbon fuel and oxidizer (neglecting intermediate steps) have been proposed (Westbrook and Dryer 1981, 1984). Using one-step chemistry,

$$CH_4 + 2O_2 \Rightarrow CO_2 + 2H_2O \tag{17}$$

or assuming three-step chemistry,

$$CH_4 + 2O_2 \Rightarrow CO + 2H_2 + 1.5O_2;\quad CO + .5O_2 \Rightarrow CO_2;\quad 2H_2 + O_2 \Rightarrow 2H_2O\,. \tag{18}$$

The reaction rate is defined using the Law of Mass Action and an Arrhenius expression for C, the specific reaction rate constant:

$$\omega = C\prod_{i=1}^{N} \sigma_i^{\nu_i} = AT^{\alpha}\exp\left(\frac{-E_a}{R_u T}\right)\sigma_{CH_4}^{a}\sigma_{O_2}^{b}\sigma_{CO}^{c}\sigma_{H_2}^{d}\sigma_{CO_2}^{e}\sigma_{H_2O}^{f} \tag{19}$$

Here, AT^{α} is the collision frequency and the exponential term is the Boltzmann factor. The exponents a through f are given in Table 1.

Table 1. Reaction Rate Equation Data

Reaction	E_a	A	a	b	c	d	e	f
Eqn. 17	30.0	8.3×10^5	–0.3	1.3	0.0	0.0	1.0	2.0
Eqn. 18, (1)	30.0	8.3×10^5	1.0	2.0	1.0	2.0	0.0	0.0
Eqn. 18, (2)	44.7	3.0×10^6	0.0	0.5	1.0	0.0	1.0	0.0
Eqn. 18, (3)	37.6	1.0×10^5	0.0	1.0	0.0	2.0	0.0	2.0

3. COMPUTATIONAL GRID

The governing equations, in finite-volume form, are solved on a finite mesh of nodes distributed in a zonal fashion around the projectile and throughout the flow field. Using this technique, sharp geometric corners and contour details are accurately represented. Figure 1 shows the projectile surface and tube surface for a 3-D mesh around the projectile. The numbers of axial, radial, and azimuthal grid nodes are 200, 25, and 66, respectively. Separate zones were placed ahead of the projectile nosetip, over the forebody, between the fins on the afterbody, and in the wake region. The mesh for an axisymmetric computation is simpler since the fins are removed; therefore, requiring only one azimuthal plane. Separate zones are generated as discussed previously. Typically, the numbers of axial and radial grid nodes are 165 and 100, respectively.

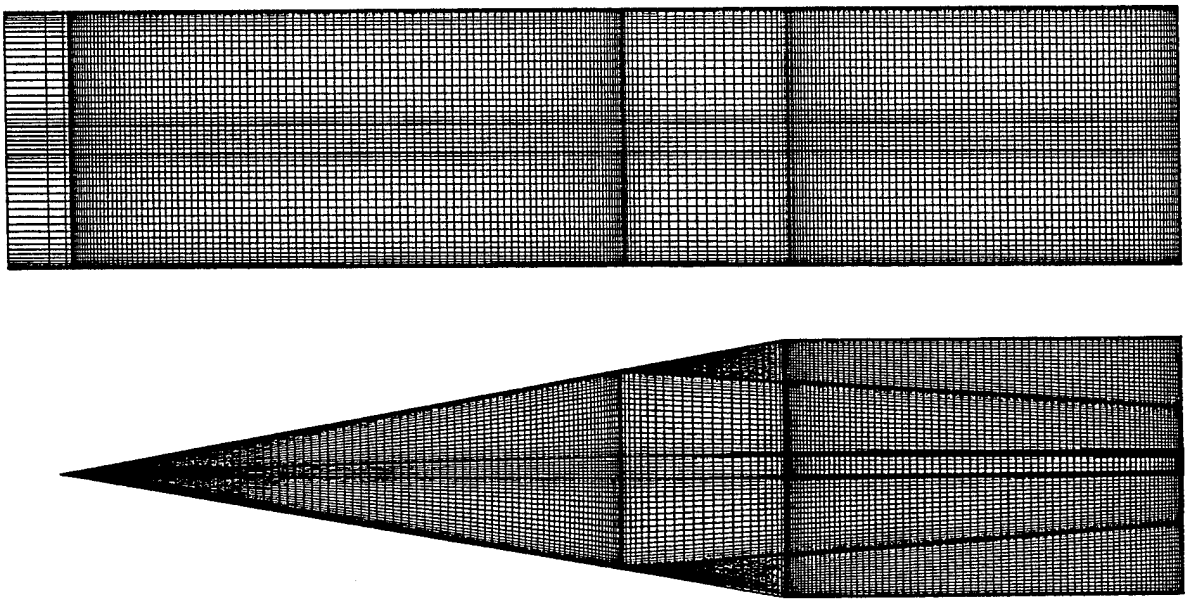

Figure 1. 3-D computational grid over surface of projectile with four fins (one hidden from view) and over surface of accelerator tube.

4. COMPUTATIONAL RESULTS

Computational simulations for the ARL 120-mm ram accelerator were performed to validate the CFD code and investigate various gasdynamic and chemical kinetic effects. Results are presented in

sections 4.1 through 4.3. Some limited 3-D numerical simulations are presented in section 4.1. CFD code validation results for axisymmetric flow are presented in section 4.2 where measured and computed tube wall pressures are compared. Time-accurate solutions are used to predict projectile performance and are compared to measured data in section 4.3.

4.1 Steady Three-Dimensional. Figure 2 shows the computed temperature contours on the projectile surface and accelerator tube surface for frozen (i.e., nonreacting) flow. The Mach number, tube charge pressure, and Reynolds number are 3.5, 51 atm and 4.3 million, respectively. In these gray-scale figures, the lighter colors correspond to hot temperatures. The forebody-afterbody junction is illustrated by a vertical black line (0.5L). Three fins are visible—top and bottom fins shown in planform and the third fin shown on edge (fin edges illustrated by two horizontal black lines). Note the hot gas temperature on the fin edge at the tip as well as on the tube surface where fin shocks intersect (whitish "X" patterns in Figure 2). Gas temperatures on the forebody (cone) surface are uniform except where the nose shock intersects the projectile after reflecting from the tube wall. Several expansion regions and shock reflections can be observed along the fin planform (Figure 2, top and bottom); a dark (cool) expansion region over the fin bevel, a bright (hot) shock impingement region at mid-planform, and a succession of weakening (gray to black color) shock reflections along the fin. A dark (cool) flow expansion is also observed on the projectile afterbody between fins. The fin-fin shock interaction seen in the CFD simulation emulates experimental observations (see Kruczynski 1994a where an experimental flow visualization via smear photograph shows combustion emanating from the fin leading edges and engulfing the projectile afterbody).

Figure 3 shows pressure distributions on the tube wall over the fin tip and between fins. High pressures at the fin tip (x/L = 0.65), between the fin and the tube wall (0.6-mm gap), as well as between the fins due to shock reflections and fin-shock intersections, are observed. Also shown in Figure 3 is a comparison between pressure computed on the tube wall for a 3-D computation (between fins) and an axisymmetric computation (projectile without fins). Pressure peaks are observed in similar locations, but of reduced magnitude for the axisymmetric case. These viscous, frozen chemistry, 3-D computations required 10 CPU hours (CRAY 2). Computations with finite-rate (three-step) kinetics required 15–20 CPU hours per case.

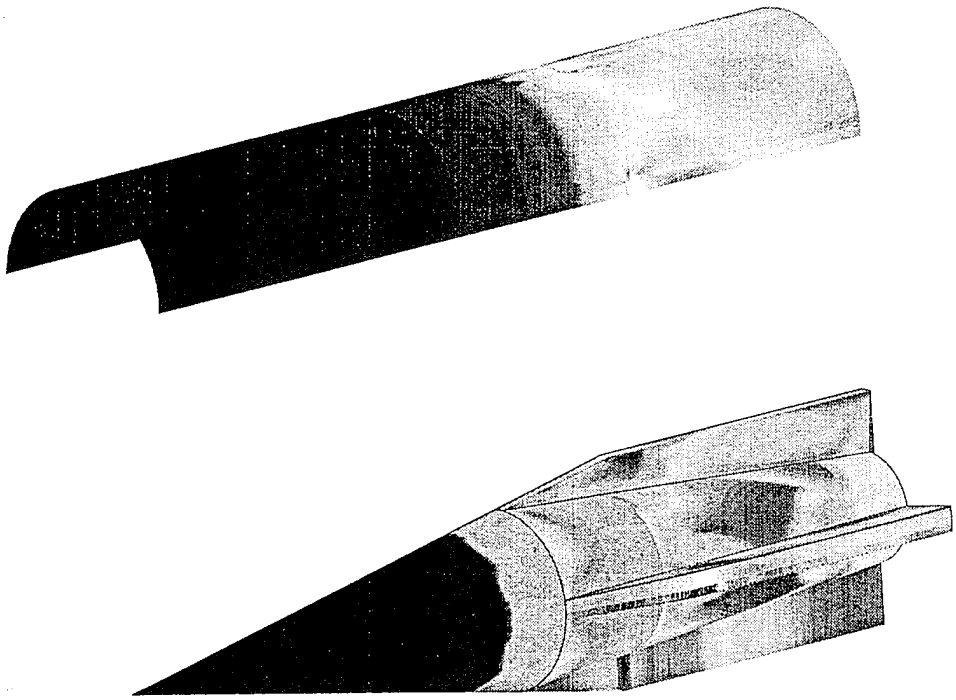

Figure 2. Gray-scale surface temperature contours for 3-D projectile (one fin shown on edge) and tube wall. Frozen chemistry, Mach number = 3.5, fill p = 51 atm, fill T = 298 K. White = 1,760 K. Black = 394 K.

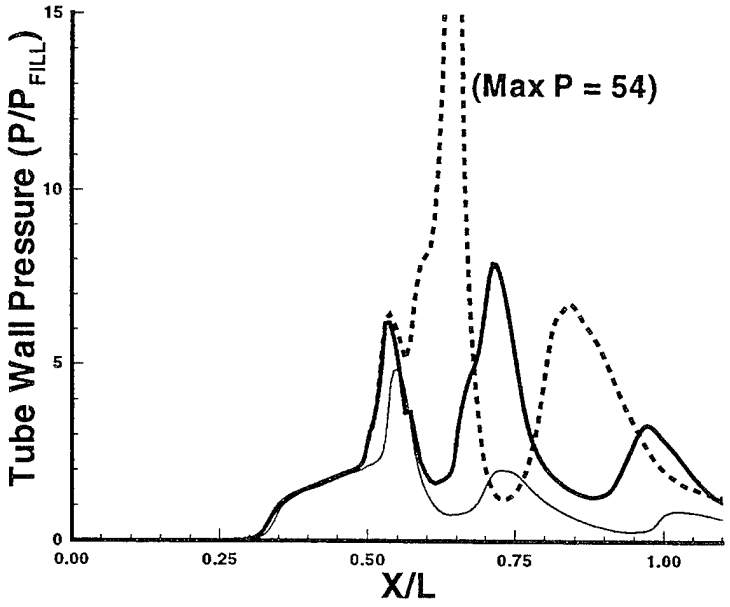

Figure 3. Computed tube wall pressures, Mach number = 3.5, fill p = 51 atm. Axisymmetric (narrow line), 3-D between fins (thick line), and 3-D over fin top (broken line).

Much can be learned by neglecting the projectile fins and investigating certain aspects of ram accelerator propulsion using axisymmetric simulations. These are the subject of the remainder of this section while further 3-D simulations will be addressed in future studies.

4.2 Steady Axisymmetric. CFD simulations were performed for conditions corresponding to shots 14, 15, 22, 23, and 25 of the ARL 120-mm ram accelerator (Kruczynski 1994a). While the gas mixture used for shot 14 consisted of nitrogen alone (i.e., inert shot), the other shots cited used the mixture described by Equation 15. The projectile was accelerated to approximately 1,200 m/s in each shot before entrance to the ram accelerator tube. This tube was pressurized to 750, 1,000, 1,250, and 1,500 psi (51, 68, 85, and 102 atm), for shots 14/15, 22, 23, and 25, respectively (gas temperature of 298 K). Pressure taps were installed at 0.3, 0.6, 1.15, 2.3, 3.46, 4.06, and 4.35 m from the accelerator entrance diaphragm and will be hereafter referred to as stations 1–7. The velocity at each station was measured using a radar technique (Kruczynski 1994a).

Figures 4–8 show the comparison of measured and computed tube wall pressure distributions above the projectile at a particular tube station and for each shot (see Nusca 1994a for further results). Figure 4 shows the results for inert (chemically frozen) shot 14 using nitrogen gas. As noted in the comparison of 3-D and axisymmetric simulations (Figure 3), locations of the pressure peaks agree with measurements, however, at a reduced magnitude. The trend in pressure peak magnitude with x/L is similar for computation and experiment. It should be noted that the obturator (not included in the computation) is in relatively close proximity to the projectile and could be affecting these pressures (shot 14 only). The relatively gradual obturator discard is a characteristic of inert shots not observed in shots through reacting mixtures (as determined by monitoring the obturator position relative to the projectile base at shot exit using a high-speed camera).

Figure 5 shows data for station 4 and shot 15, the lowest pressure shot. The first substantial pressure rise ($x/L \approx 0.55$) is slightly (5%) overpredicted. This peak is due to the first impact of the nose shock reflected from the tube wall to the projectile surface and back to the tube wall again. Computations indicate some level of reaction at this point (Nusca 1994a). The second predominant peak occurs nearly at the end of the projectile ($x/L = 1$) and is either predicted in the proper location or rearward; the magnitude is, in some cases, slightly over or under predicted. Pressures downstream of the projectile ($x/L > 1$) are generally computed near the measured magnitude, but without high-frequency oscillations. Several theories concerning the absence of pressure oscillations in these computations are under

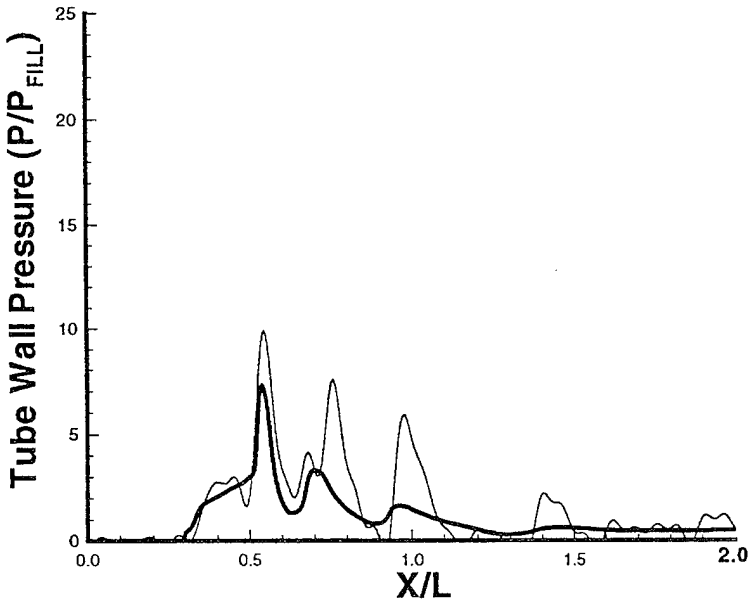

Figure 4. Tube wall pressures, shot 14, station 5, inert flow, Mach number = 3.3, fill p = 51 atm. Measured (narrow line) and computed (thick line).

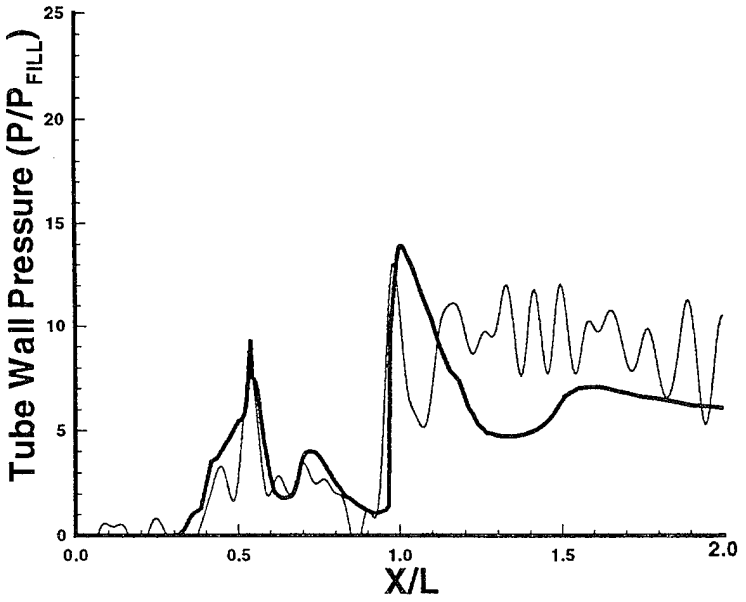

Figure 5. Tube wall pressures, shot 15, station 4, Mach number = 3.45, fill p = 51 atm. Measured (narrow line) and computed (thick line).

investigation, including the time-averaging technique, turbulence model employed, and the assumption of a rigid accelerator tube.

Figures 6 and 7 show data and computations for shots 22 and 23, each representing subsequently higher tube fill pressures. Results for station 4 (middle of the tube) are shown and can be compared to station 4 (Figure 5) for the low-pressure shot. The first major pressure rise ($x/L \approx 0.55$) is preceded by a smaller pressure spike, to some degree replicated by the computation. More pressure spikes are recorded between $x/L = 0.55$ and $x/L = 1$ compared to shot 15. As with shot 15, large pressure rises occur near the end of the projectile ($x/L = 1$) and are simulated to a better degree for shot 22 (Figure 6).

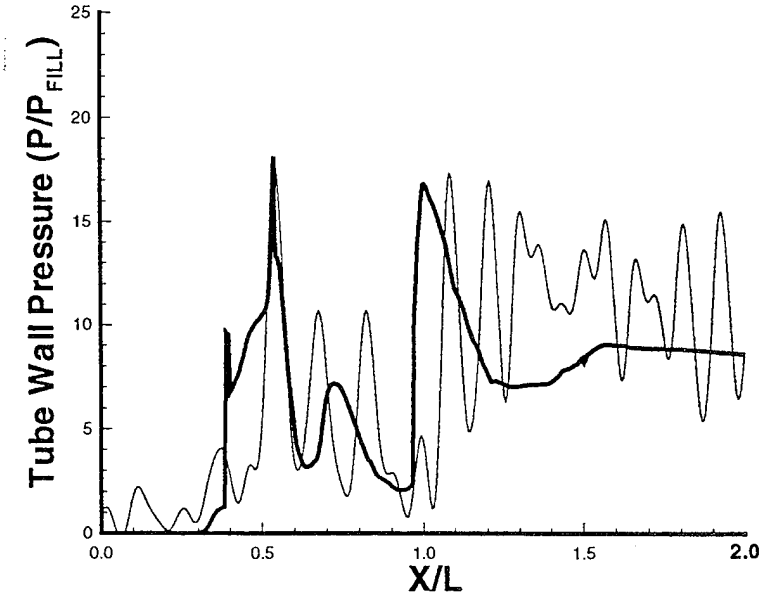

Figure 6. Tube wall pressures, shot 22, station 4, Mach number = 3.44, fill p = 68 atm. Measured (narrow line) and computed (thick line).

Figure 8 represents shot 25 using the highest tube fill pressure. Comparing this data (for station 1) with that for all other shots (for station 4) we find a trend toward similar magnitude for the first pressure spike, located near $x/L = 0.55$, and the second spike, located near $x/L = 1$. Both locations contain reacting flow and indicate combustion moving onto the forebody. Data recorded for subsequent stations (Nusca 1994a) for shot 25 showed an "unstart" (i.e., combustion ahead of the projectile, see Kruczynski 1994a).

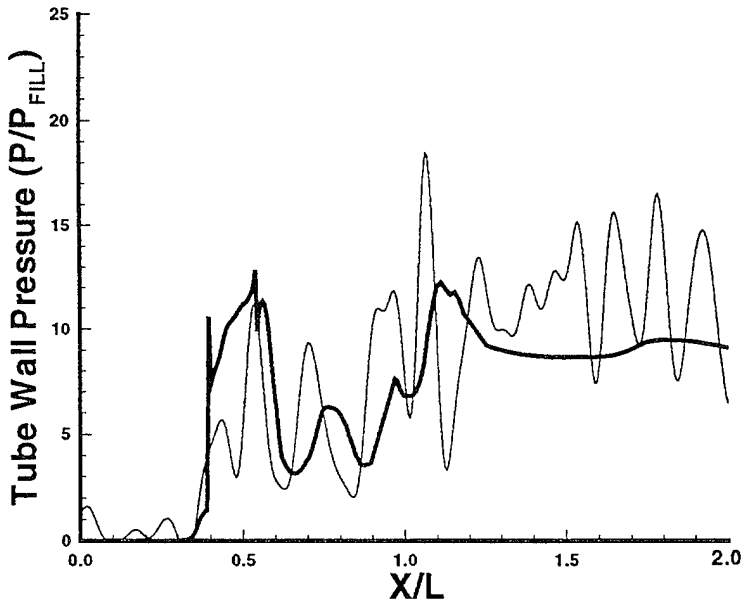

Figure 7. Tube wall pressures, shot 23, station 4, Mach number = 3.72, fill p = 85 atm. Measured (narrow line) and computed (thick line).

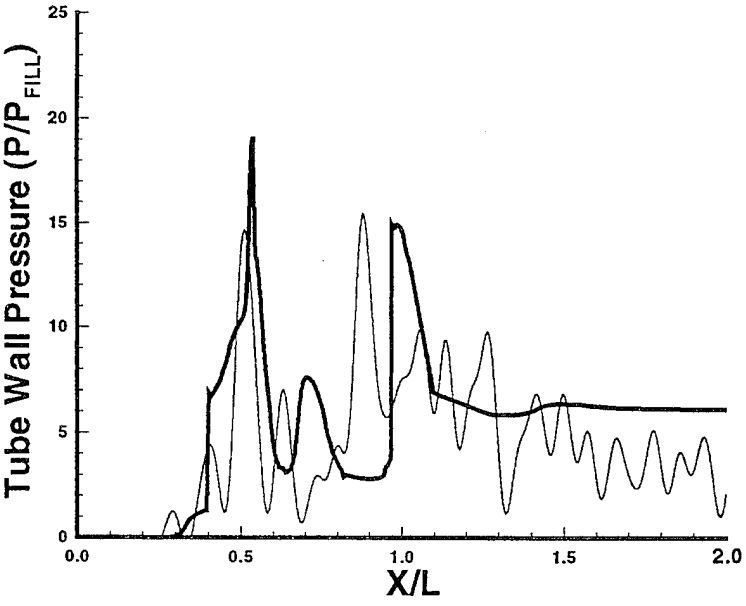

Figure 8. Tube wall pressures, shot 25, station 1, Mach number = 3.32, fill p = 102 atm. Measured (narrow line) and computed (thick line).

The discussion and conclusions previously presented are supported by flow field visualization accomplished by plotting computed temperature fields for each shot. Figures 9 and 10 correspond to conditions for shot 14 station 5 (Mach = 3.3) and shot 15 station 4 (Mach = 3.45), respectively. In these gray-scale figures, the lighter colors correspond to cool temperatures. Figure 9, inert shot, shows the projectile nose shock reflecting from the tube wall, impinging near the projectile forebody/afterbody junction, and subsequently reflecting and weakening downstream. High-temperature boundary layers are observed on the projectile and tube walls. Figure 10, combustion shot, shows wide regions of high-temperature gas caused by shocks and combustion, superimposed. Note, combustion occurs in the projectile and tube wall boundary layers as well; rapid boundary layer thickening caused by shock wave impingement is evident. Some localized combustion occurs in the forebody boundary layer. Results for higher pressure shots (Nusca 1994b) show that extensive combustion between the projectile forebody and tube wall becomes more predominant with increasing freestream pressure. In addition, increased projectile acceleration causes the nose shock to reflect further rearward on the tube wall, combustion to move from the second shock reflection to the first, and combustion in the forebody boundary layer to move forward. These effects shift high pressure to the forebody where drag is generated, counteracting thrust generated by high pressure on the afterbody.

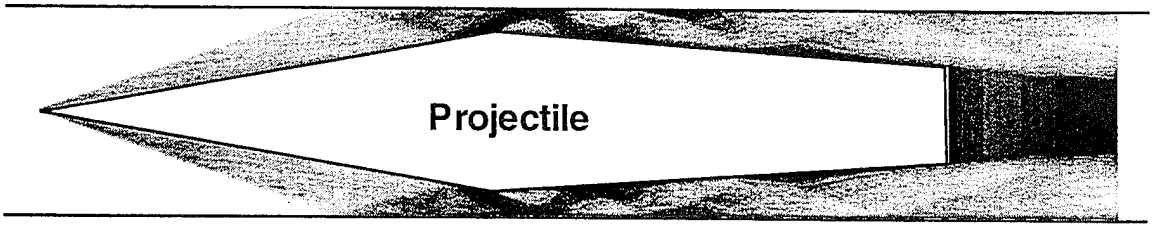

Figure 9. Gray-scale temperature contours, shot 14, station 5, inert flow, Mach number = 3.3, fill p = 51 atm. White = 298 K. Black = 417 K.

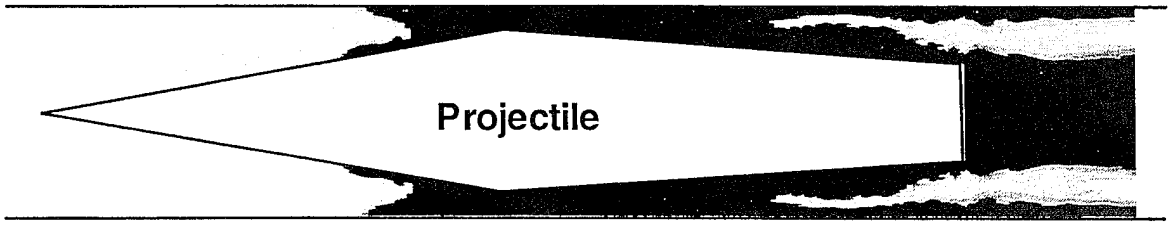

Figure 10. Gray-scale temperature contours, shot 15, station 4, Mach number = 3.45, fill p = 51 atm. White = 298 K. Black = 745–2,700 K.

4.3 Unsteady Axisymmetric. Time-accurate CFD simulations are reported for conditions corresponding to shot 27 of the ARL 120-mm ram accelerator (Kruczynski 1994a). The projectile was injected at approximately 1,250 m/s (Mach number = 3.5) into the accelerator tube filled with a gaseous mixture (see Equation 15) at 300 K and pressurized to 750 psi (50 atm). The mixture has a sound speed of 361 m/s, a Chapman-Jouget detonation speed of 1,448 m/s, and a precombustion γ of 1.379 (see Liberatore 1994). Pressures on the accelerator tube wall were collected at 11 ports located from 0.3 to 9.1 m from the entrance diaphragm. Doppler radar was used to obtain a continuous in-bore velocity-time history of the projectile. The CFD simulation was started with the entrance of the projectile/obturator combination into the accelerator tube at t = 20.05 ms with specified velocity (1,256.4 m/s) and obturator back pressure (4,000 psi). Obturator back pressure was measured using a pressure guage as the projectile entered the accelerator. The projectile fins were neglected so that axisymmetric simulations could be used. The flow field equations (Equation 1) were then solved in a time-accurate fashion along with a force computation for the projectile and obturator, individually. The velocity of the projectile and the relative separation between the projectile base and obturator were updated for each time step (0.2 ms) using the computed, time-dependent force and given masses. The backpressure on the obturator due to the conventional charge was assumed to be ambient after 20.45 ms. When the obturator is greater than five projectile lengths downstream of the projectile base, its influence on the projectile flow field is negligible. A downstream outflow condition is then prescribed one projectile body length behind the projectile.

Figures 11 and 12 show the computed time sequence of projectile obturator separation in terms of gas H_2O mass fraction and flow field Mach number, respectively. Water is a major product for the reaction given by Equations 17 and 18, thus illustrating regions of significant combustion activity. For Figure 11, white corresponds to the absence of H_2O in the flow field, while dark-grey corresponds to a water mass fraction of 0.1. For Figure 12, black corresponds to subsonic flow. Flow stagnation on the obturator, when in close proximity to the projectile, causes both a normal shock and a combustion front to occur on the projectile. The combustion front is located on the projectile forebody while the normal shock is located on the afterbody. Flow between the combustion front and the normal shock is slightly supersonic. As the obturator is pushed further back from the projectile (the last frame of Figures 11 and 12 corresponds to an obturator location of 1.47 m or 2.81 projectile lengths, behind the projectile base), the normal shock moves rearward and is eventually positioned behind the projectile. At this point, the projectile is in fully supersonic flight. Combustion occurs at the projectile-afterbody junction due to shock heating, in the projectile and tube wall boundary layers due to stagnation heating, and downstream of the normal shock traveling behind the projectile. This normal shock, which also initiates combustion, is now

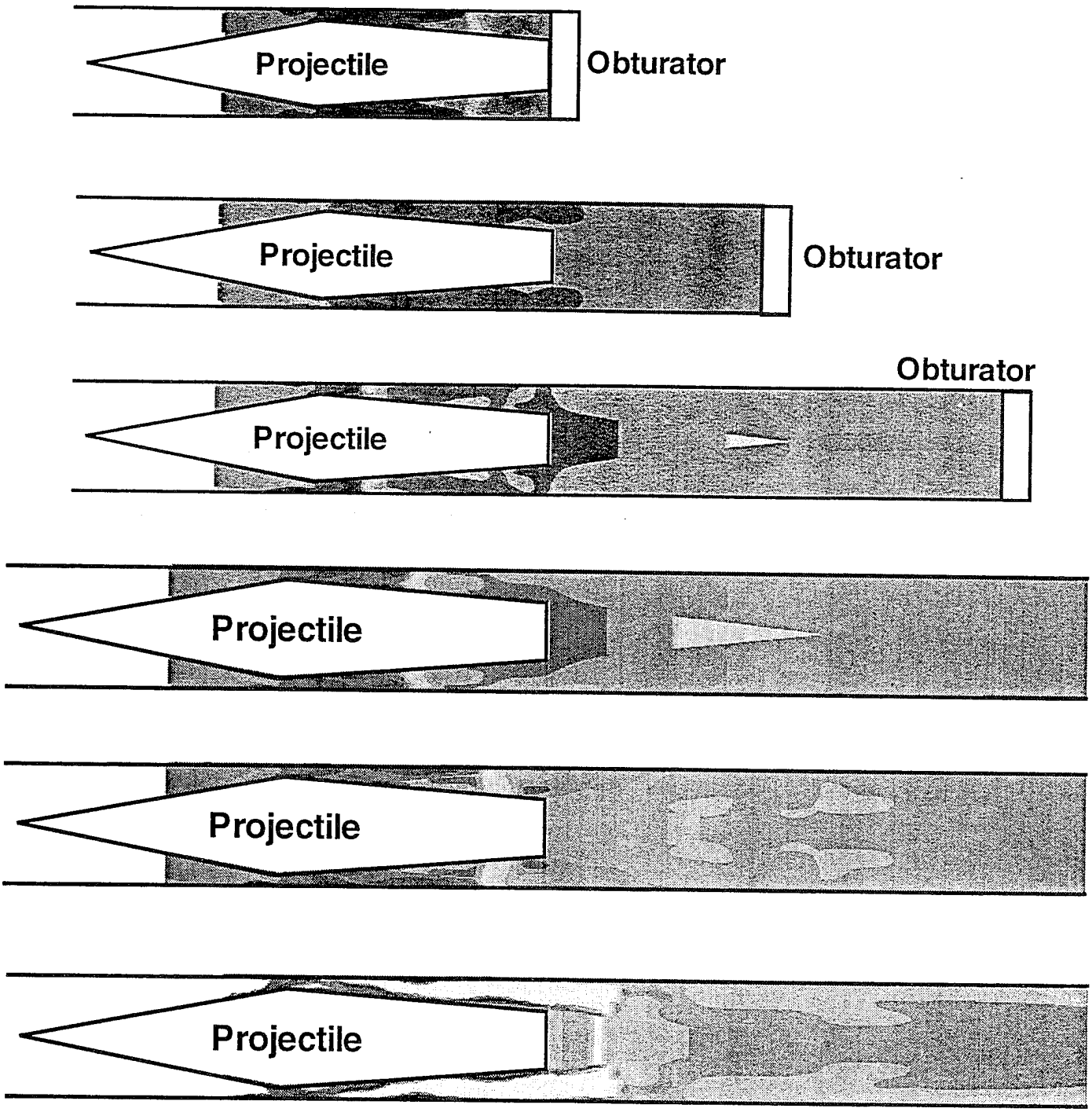

Figure 11. Flow field H_2O mass fraction contours ($0 \leq \sigma \leq 0.1$). Standard mixture at 51 atm. Time sequence from 20.05 ms to 21.05 ms, 0.2-ms interval. Computed projectile velocities: 1,256, 1,267, 1,289, 1,299, 1,305, and 1,310 m/s. Computed obturator locations: 0, 0.433, 0.961, 1.51, 2.1, and 2.81 m from projectile base.

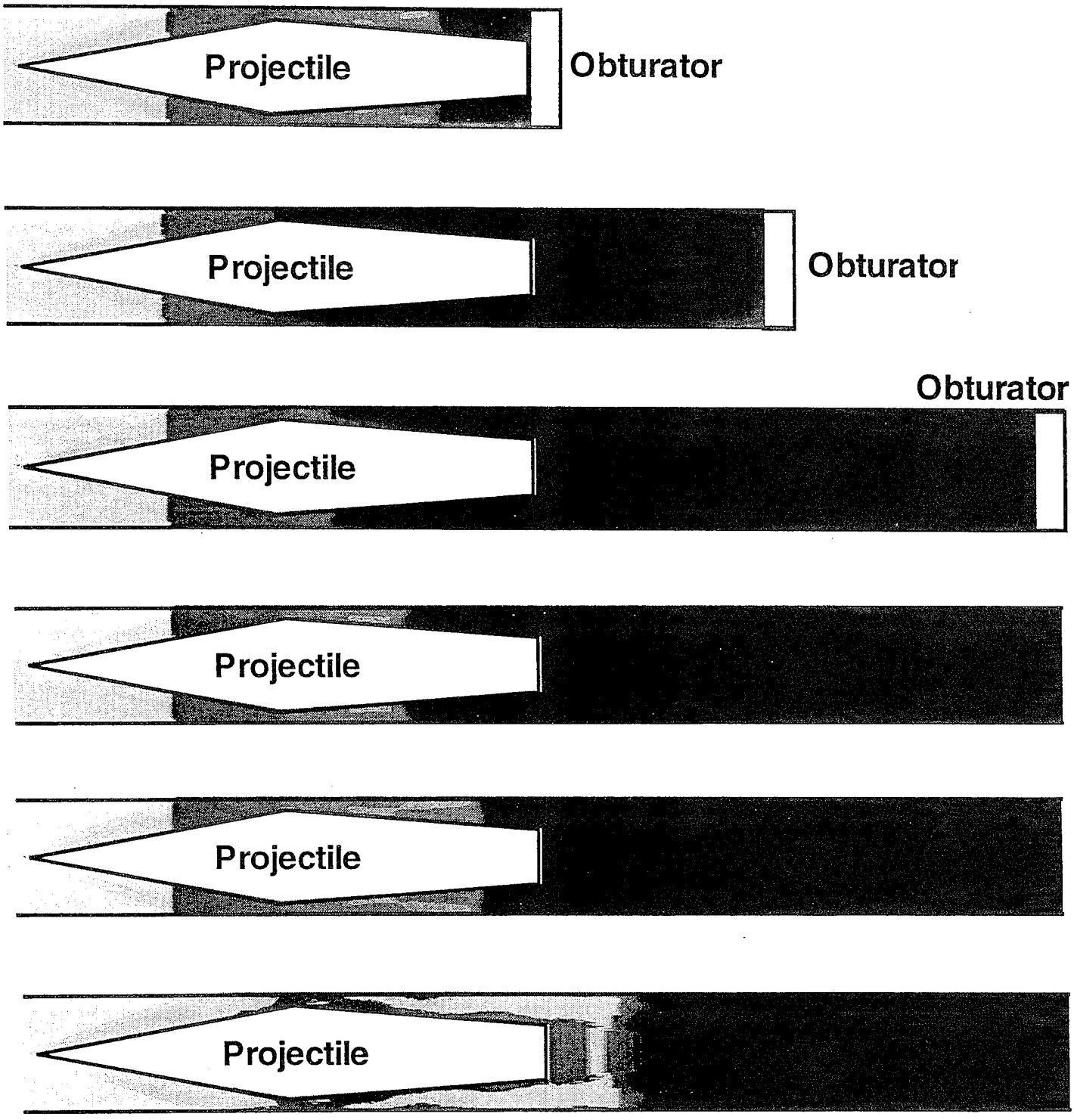

Figure 12. Flow field Mach number contours (0.09 ≤ Mach number ≤ 3.9). Standard mixture at 51 atm. Time sequence from 20.05 ms to 21.05 ms, 0.2-ms interval. Computed projectile velocities: 1,256, 1,267, 1,289, 1,299, 1,305, and 1,310 m/s. Computed obturator locations: 0, 0.433, 0.961, 1.51, 2.1, and 2.81 m from projectile base.

driven by the obturator (i.e., a piston). Due to the high combustion pressures on the side facing the projectile as well as the relieved backpressure, the obturator is moving slower that the projectile (this computational simulation can be compared to the experimentally photographed sequence, see Kruczynski 1994a).

Figure 13 shows the measured projectile velocity-time history. The projectile velocity was measured using a Doppler radar positioned outside the accelerator and beamed down the tube bore using a sacrificial mirror. Tube-mounted transducers were used to measure the projectile pressure signature as it passed each station. The computer simulation shows a jump in the velocity relative to measurements just beyond station 2. Thereafter the computed projectile velocity was fairly constant at 2.3% above measurements. The large projectile thrust computed near station 2 is due to a higher than measured pressure on the projectile afterbody. It is thought that perhaps the obturator is tilted (i.e., the obturator length is such that the obturator can spin within the tube cross section), thus relieving some pressure from behind the projectile. In the computations, the obturator is constrained to move perpendicular to the projectile, whereas obturator tilting has been observed in experiments (Kruczynski 1994b).

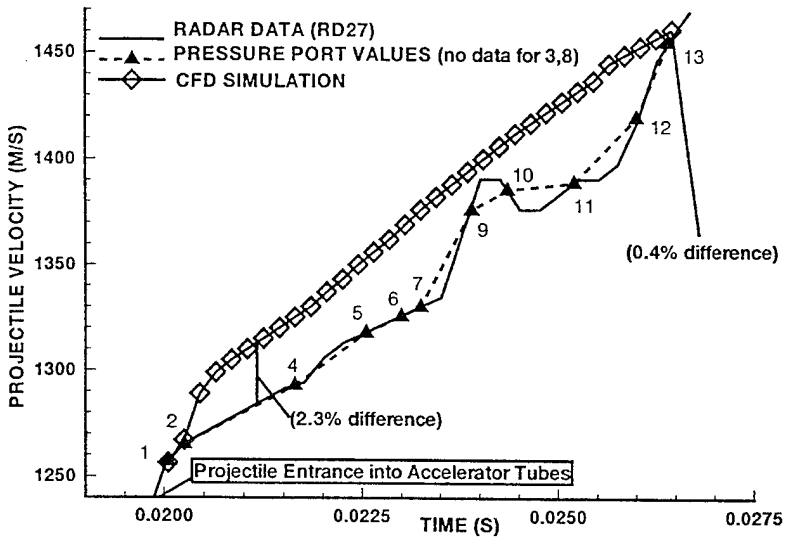

Figure 13. computed and measured projectile velocity vs. time of flight for shot 27. Mixture: $3CH_4 + 2O_2 + 10N2$ at 51 atm and 300 K fill conditions.

Figure 14 shows a comparison of the measured and computed tube wall pressure distribution at station 2. Figure 14 also shows results for station 9 where better agreement is obtained. A possible cause for discrepancy in computed pressures are flow transients introduced by diaphragm rupture and the aforementioned obturator tilting that are not included in the simulation.

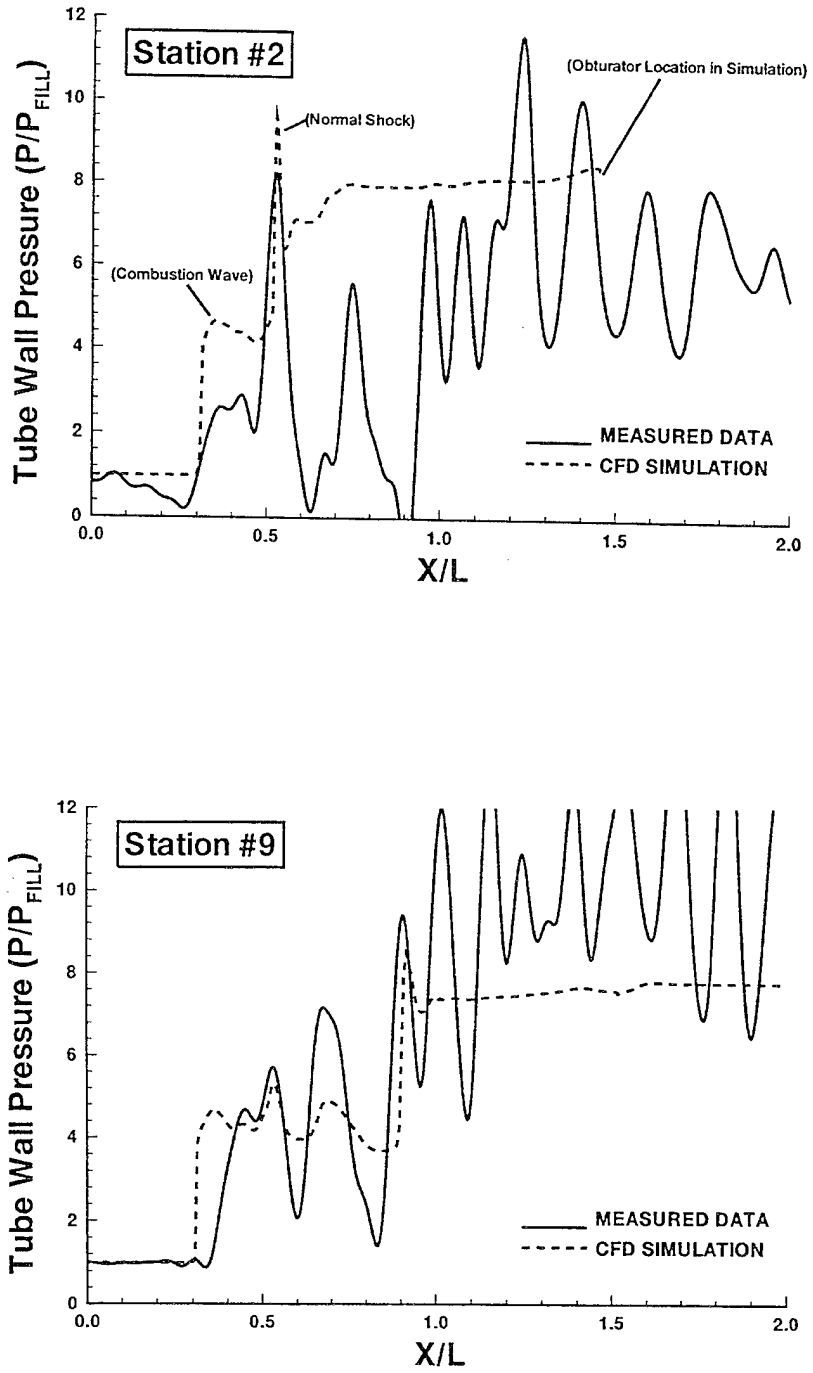

Figure 14. Computed and measured tube wall pressure distributions for shot 27, station numbers 2 and 9.

5. CONCLUSIONS

Computational fluid dynamics simulations of the ram accelerator show that shock waves originating from the projectile nosetip and reflecting from the accelerator tube wall provide sufficient heating to sustain combustion of the gas mixture. Wall boundary layers on the projectile forebody and afterbody sections, as well as on the accelerator tube, provide locally reacting regions. On the afterbody, combustion is generally confined to these wall layers that thicken with distance. Unsteady simulations show stagnation of the combustible gas on the projectile obturator, which causes formation of a normal shock and a combustion wave in the flow field. As the obturator is gasdynamically discarded, the normal shock trails behind the projectile and the combustion wave collapses into shock-induced combustion on the projectile. This effect has been observed computationally as well as with experimental flow visualization. With the obturator sufficiently downstream, the projectile accelerates at supersonic speeds. Projectile velocity through the accelerator can be predicted.

INTENTIONALLY LEFT BLANK.

6. REFERENCES

Anderson, D. A., J. C. Tannehill, and R. H. Pletcher. Computational Fluid Mechanics and Heat Transfer, New York: Hemisphere Publishing Corp., McGraw-Hill Book Co., 1984.

Anderson, W. R., and A. J. Kotlar. "Detailed Modeling of CH_4/O_2 Combustion for Hybrid In-Bore Ram Propulsion (HIRAM) Application." Proceedings of the 28th JANNAF Combustion Meeting, CPIA Pub. 573, vol. 2, pp. 417–426, 1991.

Baldwin, B. S., and H. Lomax. "Thin Layer Approximation and Algebraic Model for Separated Turbulent Flows," AIAA Paper No. 78-257, January 1978.

Chakravarthy, S. R., K. Y. Szema, U. C. Goldberg, J. J. Gorski, and S. Osher. "Application of a New Class of High Accuracy TVD Schemes to the Navier-Stokes Equations," AIAA Paper No. 85-0165, January 1985.

Drummond, J. P., C. Rogers, and M. Y. Hussaini. "A Numerical Model for Supersonic Reacting Mixing Layer." Computer Methods in Applied Mechanics and Engineering, vol. 64, pp. 16–32, 1987.

Giraud, M., J-F. Legendre, and G. Simon. "Ram Acceleration at ISL; First Experiments in 90mm Caliber." Proceedings of the 42nd Meeting of the Aeroballistic Range Association, Adelaide, Australia, pp. 12–16, 1991.

Goldberg, U. C. "Separated Flow Treatment with a New Turbulence Model." AIAA Journal, vol. 24, No. 10, pp. 1711–1713, 1986.

Gruschka, H. D., and F. Wecken. Gasdynamic Theory of Detonation, New York: Gordon and Breach Science Publishers, 1971.

Hertzberg, A., A. P. Bruckner, and D. W. Bogdanoff. "Ram Accelerator: A New Chemical Method for Accelerating Projectiles to Ultrahigh Velocities." AIAA Journal, vol. 26, No. 2, pp. 195–203, 1988.

Hirschfelder, J. O., C. F. Curtiss, and R. Bird. Molecular Theory of Gases and Liquids, New York: John Wiley & Sons, 1954.

Hosangadi, A., B. J. York, N. Sinha, and S. M. Dash. "Progress in Transient Interior Ballistic Flow field Simulations Using Multi-Dimensional Upwind/Implicit Numerics." AIAA Paper No. 93-1915, June 1993.

Kruczynski, D. L. "Flow Visualization of Steady and Transient Combustion in a 120-MM Ram Accelerator." AIAA Paper No. 94-3344, June 1994a.

Kruczynski, D. L. "Experiments in a 120-MM Ram Accelerator Including Flow Visualization." Proceedings of the 31st JANNAF Combustion Subcommittee Meeting, CPIA Pub. 620, vol. 1, pp. 102–110, 1994b.

Li, C., A. M. Landsberg, K. Kailasanath, E. S. Oran, and J. P. Boris. "Numerical Simulations of Reactive Flows in Ram Accelerators." Proceedings of the 29th JANNAF Combustion Meeting, CPIA Pub. 593, vol. 1, pp. 279–288, 1992.

Liberatore, F. "Ram Accelerator Performance Calculations Using a Modified Version of the NASA CET89 Equilibrium Chemistry Code." ARL-TR-647. U.S. Army Research Laboratory, Aberdeen Proving Ground, MD, December 1994.

Nusca, M. J. "Reacting Flow Simulation for a Large Scale Ram Accelerator." AIAA Paper No. 94-2963, June 1994a.

Nusca, M. J. "Numerical Simulation of Ram Accelerator Performance Including Transient Effects During Initiation of Combustion and Sensitivity Studies." Proceedings of the 31st JANNAF Combustion Subcommittee Meeting, CPIA Pub. 620, vol. 1, pp. 111–118, 1994b.

Palaniswamy, S., and S. R. Chakravarthy. "Finite Rate Chemistry for USA Series Codes: Formulation and Applications." AIAA Paper No. 89-0200, January 1989.

Palaniswamy, S., D. K. Ota, and S. R. Chakravarthy. "Some Reacting-Flow Validation Results for USA-Series Codes." AIAA Paper No. 91-0583, January 1991.

Reif, F. Fundamentals of Statistical and Thermal Physics, New York: McGraw-Hill Book Company, 1965.

Roe, P. L. "Approximate Riemann Solvers, Parameter Vectors, and Difference Schemes." Journal of Computational Physics, vol. 43, pp. 357–372, 1981.

Smith, J. M., and H. C. Van Ness. Introduction to Chemical Engineering Thermodynamics, Fourth Edition, New York: McGraw-Hill Book Company, 1987.

Smith, W., and R. Missen. Chemical Reaction Equilibrium Analysis, New York: John Wiley & Sons, 1982.

Smeets, G., F. Seiler, G. Patz, and J. Srulijes. "First Results Obtained in a 30mm Caliber Scram Accelerator Using a Rail Tube For Cylindrical Projectiles." Proceedings of the 25th International Symposium on Combustion, Irvine, CA, pp. 21–35, 1994.

Soetrisno, M., S. T. Imlay, and D. W. Roberts. "Numerical Simulations of the Transdetonative Ram Accelerator Combusting Flow field on a Parallel Computer." AIAA Paper No. 92-3249, July 1992.

Stull, D. R., and H. Prophet. "JANNAF Thermochemical Tables." NSRDS-Rept. 37, Second ed., National Bureau of Standards, June 1971.

Westbrook, C. K., and F. L. Dryer. "Simplified Reaction Mechanisms for the Oxidation of Hydrocarbon Fuels in Flames." Combustion Science and Technology, vol. 27, pp. 31–43, 1981.

Westbrook, C. K., and F. L. Dryer. "Chemical Kinetic Modeling of Hydrocarbon Combustion." Progress in Energy Combustion Science, vol. 10, pp. 1–57, 1984.

Wilke, C. R. "A Viscosity Equation for Gas Mixtures." Journal of Chemistry and Physics, vol. 18, No. 4, pp. 517–519, 1950.

Yungster, S., and M. J. Rabinowitz. "Computation of Shock-Induced Combustion Using a Detailed Methane-Air Mechanism." Journal of Propulsion and Power, vol. 10, no. 5, pp. 609–617, 1994.

LIST OF SYMBOLS

b	covolume
c_p	specific heat capacity, constant p
c_v	specific heat capacity, constant volume
C	specific reaction rate constant
D	mass diffusion coefficient
e	specific total internal energy
E_a	activation energy
F, G	flux vectors (Equation 1)
g	Gibbs energy per mole
h	molar specific enthalpy
i	i-th species
L	total length of projectile
m	mixture quantity
M	molecular weight
n	number of moles
N	total number of species
p	static pressure
Pr	Prandtl number
Q	heat content of the mixture
R	specific gas constant, $(\gamma - 1)c_p/\gamma$
R_u	universal gas constant, RM_m
Sc	Schmidt Number, $\mu_m/\rho D$
t	time
T	static temperature
u	axial velocity
v	radial velocity
U	magnitude of the local velocity vector
V	specific volume $(1/\rho)$
W	dependent variable vector (Equation 1)
x, y	cartesian coordinates
X	species mole fraction

γ	ratio of specific heats, c_p/c_v
ΔH_f	enthalpy of formation
κ	heat transfer coefficient
μ	molecular viscosity
ν	stoichiometric coefficient
ρ	density
σ	species mass fraction
τ	shear stress tensor
ω	chemical production term (Equation 19)
Ω	source term vector (Equation 1)

NO. OF COPIES	ORGANIZATION
2	ADMINISTRATOR DEFENSE TECHNICAL INFO CTR ATTN DTIC DDA CAMERON STATION ALEXANDRIA VA 22304-6145
1	DIRECTOR US ARMY RESEARCH LAB ATTN AMSRL OP SD TA 2800 POWDER MILL RD ADELPHI MD 20783-1145
3	DIRECTOR US ARMY RESEARCH LAB ATTN AMSRL OP SD TL 2800 POWDER MILL RD ADELPHI MD 20783-1145
1	DIRECTOR US ARMY RESEARCH LAB ATTN AMSRL OP SD TP 2800 POWDER MILL RD ADELPHI MD 20783-1145
	ABERDEEN PROVING GROUND
5	DIR USARL ATTN AMSRL OP AP L (305)

NO. OF COPIES	ORGANIZATION
2	HQDA ATTN SARD TR MS K KOMINOS DR R CHAIT WASHINGTON DC 20310-0103
1	SDOP TNI ATTN L H CAVNEY PENTAGON WASHINGTON DC 20301-7100
6	COMMANDER USA ARDEC ATTN SMCAR AET A R DEKLEINE R KLINE R BOTTICELLIE H HUDGINS J GRAU S KAHN PICATINNY ARSENAL NJ 07806-5001
1	COMMANDER USA ARDEC ATTN SMCAR CCH V P VALENTI PICATINNY ARSENAL NJ 07806-5001
1	COMMANDER US ARMY RESEARCH OFFICE ATTN TECHNICAL LIBRARY PO BOX 12211 RESEARCH TRIANGLE PARK NC 27709-2211
1	COMMANDER US ARMY RESEARCH OFFICE ATTN D MANN PO BOX 12211 RESEARCH TRIANGLE PARK NC 27709-2211
1	DIRECTOR US ARMY RESEARCH OFFICE ATTN AMXRO MCS K CLARK PO BOX 12211 RESEARCH TRIANGLE PARK NC 27709-2211
1	DIRECTOR US ARMY RESEARCH OFFICE ATTN AMXRO RT IP LIBRARY SERVICES PO BOX 12211 RESEARCH TRIANGLE PARK NC 27709-2211

NO. OF COPIES	ORGANIZATION
1	COMMANDER NAVAL RESEARCH LABORATORY ATTN TECHNICAL LIBRARY WASHINGTON DC 20375-5000
4	COMMANDER NAVAL RESEARCH LABORATORY ATTN CODE 4410 K KAILASANATH J BORIS E ORAN C LI WASHINGTON DC 20375-5000
2	COMMANDER NAVAL SURFACE WARFARE CENTER ATTN DR F MOORE MR G GRAFF DAHLGREN VA 22448
7	COMMANDER NAVAL SURFACE WARFARE CENTER ATTN T C SMITH K RICE S MITCHELL S PETERS J CONSAGA C GOTZMER TECHNICAL LIBRARY INDIAN HEAD MD 20640-5000
2	COMMANDER NSWC WHITE OAK LABS ATTN CODE R44 DR A WARDLAW K24 B402 12 DR W YANTA SILVER SPRING MD 20903-5000
1	USAF WRIGHT AERONAUTICAL LABS ATTN AFWAL FIMG DR J SHANG WRIGHT PATTERSON AFB OH 45433-6553
1	AFOSR NA ATTN J TISHKOFF BOLLING AFB 20332-6448
3	AIR FORCE ARMAMENT LABORATORY ATTN AFATL FXA S C KORN B SIMPSON S BELK EGLIN AFB FL 32542-5434

NO. OF COPIES	ORGANIZATION
2	WL MNSH ATTN R DRABCZUK D LITTRELL EGLIN AFB FL 32542-5434
1	LOS ALAMOS NATIONAL LABORATORY ATTN B HOGAN MS G770 LOS ALAMOS NM 87545
2	DIRECTOR SANDIA NATIONAL LABORATORIES ATTN DIV 1554 DR W OBERKAMPF DIV 1554 DR F BLOTTNER ALBUQUERQUE NM 87185
4	DIRECTOR NASA LANGLEY RESEARCH CENTER ATTN TECH LIBRARY D M BUSHNELL DR M J HEMSCH DR J SOUTH LANGLEY STATION HAMPTON VA 23665
2	DIRECTOR NASA LANGLEY RESEARCH CENTER ATTN MS 408 W SCALLION D WITCOFSKI HAMPTON VA 23605
1	DIRECTOR NASA AMES RESEARCH CENTER ATTN MS 227 8 L SCHIFF MOFFETT FIELD CA 94035
5	DIRECTOR NASA AMES RESEARCH CENTER ATTN MS 258 1 D CHAUSSEE MS 258 1 T HOLST MS 258 1 P KUTLER MS 258 1 P BUNING MS 258 1 M RAI MOFFETT FIELD CA 94035
1	UNITED STATES MILITARY ACADEMY DEPARTMENT OF MECHANICS ATTN LTC ANDREW L DULL WEST POINT NY 10996

NO. OF COPIES	ORGANIZATION
1	UNIVERSITY OF CALIFORNIA DEPT OF AMES ATTN C SESHADRI LA JOLLA CA 92093-0310
1	UNIVERSITY OF CALIFORNIA DAVIS DEPT OF MECHANICAL ENGINEERING ATTN PROF H A DWYER DAVIS CA 95616
1	MASSACHUSETTS INST OF TECH ATTN TECH LIBRARY 77 MASSACHUSETTS AVE CAMBRIDGE MA 02139
1	VA POLYTECHNIC INST & STATE UNIV DEPT OF AEROSPACE & OCEAN ENGRG ATTN DR C H LEWIS BLACKSBURG VA 24061
1	ADVANCED TECH CTR ARVIN CALSPAN AERODYNAMICS RESEARCH DEPT ATTN DR M S HOLDEN PO BOX 400 BUFFALO NY 14225
1	THE PENNSYLVANIA STATE UNIVERSITY DEPT OF AEROSPACE ENGRG ATTN DR G S DULIKRAVICH UNIVERSITY PARK PA 16802
3	THE PENNSYLVANIA STATE UNIVERSITY DEPT OF MECHANICAL ENGRG ATTN V YANG K KUO C MERKLE UNIVERSITY PARK PA 16802-7501
1	UNIVERSITY OF ILLINOIS AT URBANA CHAMPAIGN DEPT OF MECHANICAL & INDUSTRIAL ENGRG ATTN DR J C DUTTON URBANA IL 61801
3	UNIVERSITY OF MARYLAND DEPT OF AEROSPACE ENGINEERING ATTN DR J D ANDERSON JR DR W MELNIK DR M LEWIS COLLEGE PARK MD 20742

NO. OF COPIES	ORGANIZATION
1	UNIVERSITY OF NOTRE DAME DEPT OF AERONAUT & MECH ENGRG ATTN PROF T J MUELLER NOTRE DAME IN 46556
1	STANFORD UNIVERSITY HIGH TEMPERATURE GAS DYNAMICS LAB ATTN R HANSON STANFORD CA 94305-3032
1	UNIVERSITY OF TEXAS DEPT OF AEROSPACE ENGRG MECHANICS ATTN DR D S DOLLING AUSTIN TX 78712-1055
1	UNIVERSITY OF DELAWARE DEPT OF MECHANICAL ENGRG ATTN DR J MEAKIN CHAIRMAN NEWARK DE 19716
1	PURDUE UNIVERSISTY SCH OF AERO & ASTRONAUTICS ATTN N MESSERSMITH WEST LAFAYETTE IN 47907-1282
1	UNIVERSITY OF WASHINGTON DEPT OF AERO & ASTRONAUTICS ATTN A BRUCKNER SEATTLE WA 98195
3	SCIENCE AND TECHNOLOGY INC ATTN D MAURIZI B LOLTMAN A GLASSER 4001 N FAIRFAX DR NO 700 ARLINGTON VA 22203-1618
1	GRUMANN AEROSPACE CORPORATION AEROPHYSICS RESEARCH DEPARTMENT ATTN DR R E MELNIK BETHPAGE NY 11714
1	AEDC CALSPAN FIELD SERVICE ATTN MS 600 DR J BENEK TULLAHOMA TN 37389
1	ARROW TECHNOLOGY ASSOC INC ATTN W HATHAWAY PO BOX 4218 SOUTH BURLINGTON VT 05401-0042

NO. OF COPIES	ORGANIZATION
1	PAUL GOUGH ASSOCIATES INC ATT P S GOUGH 1048 SOUTH ST PORTSMOUTH NH 03801-5423
2	PRINCETON COMBUSTION RESEARCH LABS INC ATTN N MER N A MESSINA PRINCETON CORP PLAZA 11 DEERPARK DR BLDG IV STE 119 MONMOUTH JUNCTION NJ 08852
1	ROCKWELL INTERNATIONAL ROCKETDYNE DIVISION ATTN BA08 R B EDELMAN 6633 CANOGA AVE CANOGA PARK CA 91303-2703
1	ROCKWELL INTERNATIONAL SCIENCE CTR ATTN DR S PALANISWAMY 1049 CAMINO DOS RIOS THOUSAND OAKS CA 91360
1	VERITAY TECHNOLOGY INC ATTN E FISHER 4845 MILLERSPORT HWY EAST AMHERST NY 14501-0305
1	META COMP TECHNOLOGIES INC ATT S CHAKRAVARTHY 650 WESTLAKE BLVD SUITE 203 WESTLAKE VILLAGE CA 91362

NO. OF
COPIES ORGANIZATION

ABERDEEN PROVING GROUND, MD

34 DIR, USARL
ATTN: AMSRL-WT-P, A. HORST
AMSRL-WT-PB,
E. SCHMIDT
B. GUIDOS
P. PLOSTINS
J. SAHU
P. WEINACHT
G. COOPER
H. EDGE
AMSRL-WT, R. FIFER
AMSRL-WT-PD, B. BURNS
AMSRL-WT-PA,
T. MINOR
M. NUSCA 7 CPS
G. WREN
T. COFFEE
J. DESPIRITO
D. KOOKER
D. KRUCZYNSKI
G. KELLER
F. LIBERATORE
P. CONROY
W. OBERLE
AMSRL-WT-W, C. MURPHY
AMSRL-WT-WB, W. D'AMICO
AMSRL-WT-NC,
R. LOTERRO
AMSRL-CI-C,
W. STUREK
C. NEITUBICZ
D HISLEY

NO. OF
COPIES ORGANIZATION

4 French-German Research Institute
of Saint Louis
ATTN: M. Giraud
G. Smeets
F. Seiler
J. Srulijes
5 Rue Du General-Cassagnou
68301 Saint-Louis FRANCE

USER EVALUATION SHEET/CHANGE OF ADDRESS

This Laboratory undertakes a continuing effort to improve the quality of the reports it publishes. Your comments/answers to the items/questions below will aid us in our efforts.

1. ARL Report Number ARL-TR-966 Date of Report February 1996

2. Date Report Received _____

3. Does this report satisfy a need? (Comment on purpose, related project, or other area of interest for which the report will be used.) _____

4. Specifically, how is the report being used? (Information source, design data, procedure, source of ideas, etc.) _____

5. Has the information in this report led to any quantitative savings as far as man-hours or dollars saved, operating costs avoided, or efficiencies achieved, etc? If so, please elaborate. _____

6. General Comments. What do you think should be changed to improve future reports? (Indicate changes to organization, technical content, format, etc.) _____

CURRENT ADDRESS

_____
Organization

_____
Name

_____
Street or P.O. Box No.

_____
City, State, Zip Code

7. If indicating a Change of Address or Address Correction, please provide the Current or Correct address above and the Old or Incorrect address below.

OLD ADDRESS

_____
Organization

_____
Name

_____
Street or P.O. Box No.

_____
City, State, Zip Code

(Remove this sheet, fold as indicated, tape closed, and mail.)
(DO NOT STAPLE)

DEPARTMENT OF THE ARMY

OFFICIAL BUSINESS

NO POSTAGE
NECESSARY
IF MAILED
IN THE
UNITED STATES

BUSINESS REPLY MAIL
FIRST CLASS PERMIT NO 0001,APG,MD

POSTAGE WILL BE PAID BY ADDRESSEE

DIRECTOR
U.S. ARMY RESEARCH LABORATORY
ATTN: AMSRL-WT-PA
ABERDEEN PROVING GROUND, MD 21005-5066